

Valley polarized current and resonant electronic transport in a non-uniform MoS₂ zigzag nanoribbon

D. Gut,¹ M. Prokop,² D. C. Sticlet,³ and M. P. Nowak⁴

¹*AGH University of Science and Technology, Faculty of Materials*

Science and Ceramics, al. A. Mickiewicza 30, 30-059 Krakow, Poland

²*AGH University of Science and Technology, Faculty of Metals Engineering and*

Industrial Computer Science, al. A. Mickiewicza 30, 30-059 Krakow, Poland

³*National Institute for Research and Development of Isotopic and*

Molecular Technologies, 67-103 Donat, 400293 Cluj-Napoca, Romania

⁴*AGH University of Science and Technology, Academic Centre for Materials and Nanotechnology, al. A. Mickiewicza 30, 30-059 Krakow, Poland*

Using the tight-binding approach we study the electronic transport in a MoS₂ zigzag ribbon with a spatially varying potential profile. Considering a ribbon with a smooth potential step in the Fermi energy regime where the transport is dominated by the edge modes we find that the conductance exhibits sharp resonances due to the resonant transport through a n-p-n junction effectively created in the structure. We show that the current carried on the wire edges can be blocked despite the metallic band-structure of the ribbon. For the Fermi energies corresponding to MoS₂ bulk conduction band we identify states of the semi-infinite wire that are polarized in the K , K' , Q valleys and exhibit the valley Hall effect distinctly visible in a non-uniform ribbon. Finally, we show that well-defined momenta of the valley polarized modes allow nearly complete valley polarization of the current in a locally gated ribbon.

I. INTRODUCTION

In recent years, after the discovery of graphene, there has been increasing interest in two-dimensional materials^{1,2}. Within this group semiconducting layers of transition metal dichalcogenides (TMDCs)³ are particularly attracting. TMDCs are materials with the formula MX₂ where M is a transition metal from the group VI (Mo, W, etc.) and X is a chalcogen (S, Se, Te). Their properties have been analyzed for over 50 years⁴ but focused initially on bulk materials. Only later it was realized that the change in the number of the atomic layers significantly alters the band structure⁵ of TMDCs. Especially, the transition from an indirect to a direct-bandgap of 1.5-2 eV is observed^{3,6} when the material becomes a monolayer. The presence of the direct-bandgap within the optical range of the energy spectrum makes monolayer TMDCs very promising materials for applications in optoelectronics^{3,7}.

One of the most exploited representative of TMDCs is the molybdenum disulfide (MoS₂) monolayer, which is a sheet of molybdenum atoms in between two layers of sulfur. Recently, impressive advances on MoS₂ samples preparation have been reported which includes the nanowire fabrication using bottom-up^{8,9}, top-down¹⁰ and etching^{11,12} techniques. Most importantly, this progress allowed for a creation of elementary nanodevices that enable studies of quantum transport. Already the electronic transport in gated TMDC monolayers¹³⁻¹⁵ or the first measurements of the conductance quantization in the split-gate quantum point contact devices^{16,17} were reported.

The physical properties of nanoscale TMDCs devices are sensitive to the termination of the structure. There are two main types of the edge termination: zigzag

and armchair which result in appearance of gapless and gapped edge modes respectively. The presence of edge modes was demonstrated experimentally in single layer small TMDCs islands¹⁸ with the zigzag-edge¹⁹⁻²¹ which are typical when MoS₂ is tailored into a nanoribbon²²⁻²⁴.

Similar to graphene, the conduction and valence band edges of a monolayer TMDCs are located at the corners of the hexagonal Brillouin zone in the K and K' points. The presence of those non-equivalent sets of points gives the charge carriers the pseudospin—valley—degree of freedom²⁵ which can be studied optically^{26,27} and may be used for information encoding and processing²⁸. While the valley polarization of the charge carriers was extensively studied for bulk monolayers much less attention was paid to its implications on the electronic transport in nanostructures. It has been shown that the valley polarization can be induced in graphene nanoribbons²⁹ or for hole charge carriers in TMDCs nanostructures³⁰ by tailoring the shape and potential profile of the structure.

The goal of this paper is to explain the transport properties of a non-uniform zigzag MoS₂ nanoribbon in the context of the valley polarization of the charge carriers. For the description of the nanostructures, where both the bulk material properties and the specific edge termination are important the common approach is to exploit tight-binding (TB) models that overcome the computational effort of DFT. The TB approach for TMDCs was used already in the studies of electronic transport which focused on the properties of strained³¹ and disordered³² wires or on spin polarization in the presence of electric³³ and exchange fields³⁴.

In this work, exploiting the TB description of a MoS₂ nanoribbon we demonstrate that, despite the finite size effects in the ribbon, the valley polarization of the charge carriers is preserved and affects the spatial symmetry of

the current flowing in the wire. By considering a ribbon with a varying potential profile, we show that even though the band structure is gapless, the flowing current can be gated out and that the conductance exhibits resonances on quasi-hole states bound to the edge. Finally we show that in the non-uniform structure a potential step can serve as valley-selective filter.

This paper is organized as follows: in Section II we introduce the model used in the calculations and describe the considered system. Section III discusses the valley polarization in a pristine ribbon along with transport properties of a gated wire. The conclusions are given in Section IV followed by Appendix where we provide details of the adopted model.

II. MODEL AND THEORY

A. Spinfull tight-binding model

In the present paper we use the real-space model developed by Silva-Guillén et. al.³⁵ which improves over a common three-band approach²⁸. It provides the accurate band structure and also the correct orbital composition of the electronic bands as compared to DFT results.

The Hamiltonian of the system is expressed as:

$$H = \sum_{i,\mu} \varepsilon_{i,\mu}^M c_{i,\mu}^\dagger c_{i,\mu} + \varepsilon_{i,\mu}^S b_{i,\mu}^\dagger b_{i,\mu} + \sum_{ij,\mu\nu} (t_{ij,\mu\nu}^{MM} c_{i,\mu}^\dagger c_{j,\nu} + t_{ij,\mu\nu}^{SS} b_{i,\mu}^\dagger b_{j,\nu}) + \sum_{ij,\mu\nu} t_{ij,\mu\nu}^{MS} c_{i,\mu}^\dagger b_{j,\nu} + H.c., \quad (1)$$

where i, j and μ, ν run over the lattice sites and atomic orbitals respectively. c_i (b_i) is the annihilation operator for Mo (S) atoms and t is the hopping coefficient.

The Hilbert space is spanned by a spin-orbital wavefunction³⁵

$$\psi^{\uparrow,\downarrow} = (d_{3z^2-r^2}, d_{x^2-y^2}, d_{xy}, p_x^S, p_y^S, p_z^A), \quad (2)$$

that describes amplitudes on orbitals of Mo and S atoms which have a dominant contribution to the orbital composition of the wave function in the bands near the energy gap. S and A are Symmetric $\frac{1}{\sqrt{2}}(p_x^t + p_x^b)$, $\frac{1}{\sqrt{2}}(p_y^t + p_y^b)$ and Antisymmetric: $\frac{1}{\sqrt{2}}(p_z^t - p_z^b)$ combinations of p -orbitals of S atoms.

The on-site terms of the Hamiltonian are

$$\epsilon_M = \begin{pmatrix} \Delta_0 & 0 & 0 \\ 0 & \Delta_2 & -is\lambda_M \\ 0 & is\lambda_M & \Delta_2 \end{pmatrix}, \quad (3)$$

and

$$\epsilon_S = \begin{pmatrix} \Delta_p + V_{pp\pi} & -is\frac{\lambda_S}{2} & 0 \\ is\frac{\lambda_S}{2} & \Delta_p + V_{pp\pi} & 0 \\ 0 & 0 & \Delta_z - V_{pp\sigma} \end{pmatrix}, \quad (4)$$

SOC	λ_M	0.086
	λ_S	0.052
Crystal Fields	Δ_0	-1.094
	Δ_2	-1.511
	Δ_p	-3.559
	Δ_z	-6.886
M-S	$V_{pd\sigma}$	3.689
	$V_{pd\pi}$	-1.241
M-M	$V_{dd\sigma}$	-0.895
	$V_{dd\pi}$	0.252
	$V_{dd\delta}$	0.228
S-S	$V_{pp\sigma}$	1.225
	$V_{pp\pi}$	-0.467

Table I. SOC parameters³⁶ and Slater-Koster parameters³⁵ used in the implementation of TB model given in eV.

where s is 1 and -1 for spin up and spin down components respectively. The hopping matrices are introduced following Refs. 34 and 35 and are given in the Appendix A. Slater-Koster parameters used in the implementation of the model are taken from fitting to *ab initio* calculations performed in Ref. 35. They are presented together with the spin-orbit coupling (SOC) parameters from Ref. 36 in Table I.

B. Considered system

Figure 1(a) presents the considered system which consists of a 10.8 nm wide MoS₂ nanoribbon connected to semi-infinite leads. The ribbon lattice is build from S and Mo sites depicted with yellow and black circles respectively. The wire is terminated by inequivalent atoms in the transverse (y) direction that define zigzag edges and is connected to two semi-infinite leads denoted with the red circles.

In this work we are mainly interested in the structures with the broken translational symmetry. We consider a local potential variation in the ribbon that experimentally can be realized by locally gating the wire. We model the potential created in the structure as a smooth potential step by including additional position-dependent on-site elements on the diagonals of Eqs. (3) and (4),

$$V_{gate} = \frac{V_g}{2} \left[\tanh \frac{x + L_b/2}{\lambda} - \tanh \frac{x - L_b/2}{\lambda} \right], \quad (5)$$

where L_b is the length of the barrier and λ sets its smoothness. For the considered model we take $\lambda = 1$ nm and $L_b = 6$ nm unless stated otherwise. The example potential profile is presented in Fig. 1(a).

We consider the electronic transport in the linear response regime and solve the scattering problem using the wave-function matching approach implemented in Kwant package³⁷. The code that implements the tight-binding model used for the calculation is available in Ref. 38.

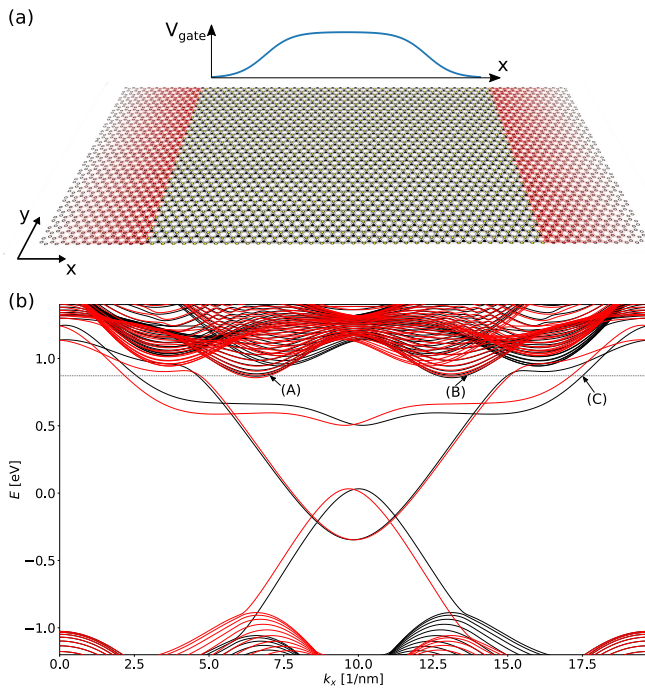


Figure 1. (a) The considered MoS₂ zigzag nanoribbon connected to two semi infinite leads (red sites). The non-uniform potential along the x -direction is plotted with the blue curve in the top of the panel. (b) Dispersion relation of a 10.8 nm wide pristine ribbon. The black and red curves correspond to the spin-up and the spin-down bands respectively. With (A), (B) and (C) we denote bands for which we calculate current and probability distributions in Fig. 4(a), (b) and (c) respectively.

III. RESULTS

A. Pristine ribbon

1. Valley-polarization of current-carrying modes

We start by considering a pristine, 10 nm long, MoS₂ zigzag ribbon. Figure 1(b) presents the dispersion relation of the wire with the black (red) curves corresponding to the spin-up (spin-down) bands. Those spin-opposite bands are split in the k -space due to the strong SOC resulting from d -orbitals of the heavy metal atoms. This is most clearly seen for the valence bands with the energies close to or less than -1 eV. The splitting is much less pronounced in the conduction bands that are present for energies exceeding 0.85 eV. In between the conduction and the valence bands there are six others making the structure metallic with no energy gap.

Let us focus on the the Fermi energy range near the conduction band minimum. In the top panels of Fig. 2 with the black curves we present zoom-ins of the dispersion relation of the ribbon. In the bottom panels with gray points we depict the Fermi contours for an infinite monolayer MoS₂ flake at the energy of 0.9445

eV. The calculation of the Fermi surface is performed by transforming the Hamiltonian Eq. (1) into the momentum space and solving the resulting eigenproblem for k_x and k_y . The bigger circles in the map form around K , K' points while the smaller ones are located around Q points. The rings around the high symmetry K and K' points are almost perfectly circular as the trigonal warping in the conduction band is much weaker than in the valence band³⁹.

In each column of Fig. 2 we demonstrate properties of a single current carrying mode i with the wave vector value denoted with the red dot in the corresponding top panel. We calculate the wave function in the scattering region $\psi_i(x, y)$ by solving the scattering problem for the incoming electron in the i 'th mode. By projecting $\psi_i(x, y)$ onto basis of plane waves we calculate the probability density in the reciprocal space as,

$$\rho_i(k_x, k_y) = \sum |\langle \psi_i(x, y) | e^{ik_x x + ik_y y} \rangle|^2, \quad (6)$$

where the summation is carried over orbital and spin degrees of freedom. The resulting probability distributions are plotted on the red colormap in the bottom panels of Fig. 2. In the two first columns we consider states that belong to the two sets of parabolas that start at the conduction band minimum. By inspecting the positions of nonzero values of probability density in the Brillouin zone depicted in the first (second) bottom panel we observe that they arrange on top of the circular contours around K' (K) points. On the other hand, the nonzero probability density for states belonging to the bands that appear at the higher energies [see the third and fourth column in Fig. 2] is close to one of the Q valley minima.

We see that the valley polarization of the charge carriers in a bulk material is preserved in a semi-infinite wire and it is translated into the valley polarization of the ribbon modes. The valley polarized modes are gathered in several sets of approximately parabolic bands with the minima at different wave vectors.

Finally, in the bottom panel of the last column we show that the density in the reciprocal space does not match any point in the Fermi contours of the bulk monolayer. This density corresponds to one of the edge modes which due to the localization on the border of the wire is delocalized in k_y space accordingly to the uncertainty principle.

Interestingly, the densities in the maps presented in Fig. 2 for the K and K' modes are distributed as a sets of dots that lie within the circular Fermi contours. To analyze further this observation let us focus on the K -polarized modes and inspect the cross-section of the probability density in the reciprocal space for positive values of k_x . We consider the subsequent modes of the transverse quantization starting from the ground state.

For each mode we obtain the corresponding k_x value at the considered Fermi energy and plot the probability distribution along k_y with the blue curves in Fig. 3. We consider only one of the spin components and the densities for the states with increasing quantization number

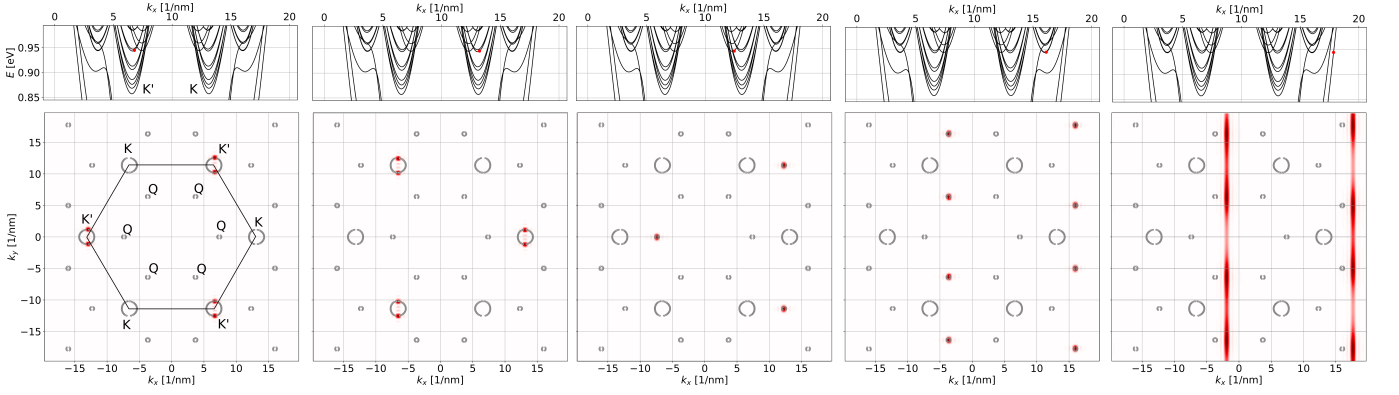


Figure 2. Top panels: the dispersion relation close to the bottom of the conduction band. Bottom panels: the grey dots depict Fermi contours of a bulk MoS₂ monolayer at the Fermi energy of 0.9455 eV. The red color map that overlays the Fermi contours corresponds to the probability density of the current carrying modes denoted with the red dots in the corresponding top panels.

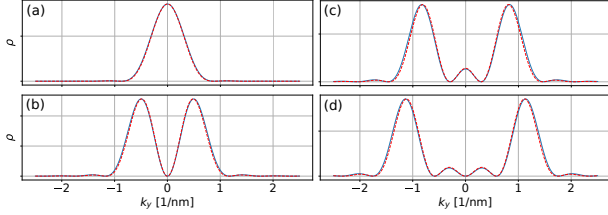


Figure 3. Blue curves depict cross-sections of the probability density in the reciprocal space calculated for K modes. Red-dashed curves show probability density of eigenstates of an infinite quantum well of the same width as the ribbon.

ranging from 1 to 4 are presented in the subsequent subplots from (a) to (d). We see that as the quantization number increases the number of maxima in the distribution rises. The shape of the probability distribution can be understood by considering a transform of a standing wave in an infinite quantum well of the width W into the momentum space. The corresponding formula for the probability density stands,

$$\rho_n(k) = \frac{W}{\pi\hbar} \left(\frac{n\pi}{n\pi + kW} \right)^2 \text{sinc}^2[1/2(n\pi - kW)], \quad (7)$$

where n is the integer index of the quantization number. We plot the resulting densities with red-dashed curves in Fig. 3. We observe that as n increases the number of maxima in the probability density distribution grows and the curves given by Eq. (7) overlay almost perfectly (up to a constant normalization factor) the distributions obtained from the numerical calculations. The distributions for the excited states have two main maxima that localize at the circular Fermi contours of the bulk material and are accompanied by a number of smaller local maxima that lie within these contours as showed in the bottom panels of Fig. 2.

2. Valley Hall effect in an open ribbon

In a 2D TMDC monolayer the time reversal symmetry guarantees that the Berry curvature flips sign between K and K' valleys, i.e. $\Omega(K) = -\Omega(K')$. This leads to the valley Hall effect where the propagating electrons acquire velocity $\mathbf{v}_\perp = -\frac{e}{\hbar\sigma} \mathbf{J} \times \Omega(K)$ perpendicular to the direction of the applied electric field that induces the current flow. Very recently signatures of the valley separation of the injected current^{40,41} were measured in the microscopic MoS₂ Hall bar devices which followed similar observation for bilayer graphene⁴².

In the present system we find the valley polarization in a nanometer-size *semi-infinite* wire. The question remains, is there a reminiscence of the valley Hall effect in the ribbon?

For a pristine wire the translational symmetry assures the invariance along the x -direction and preventing the current from drifting in the transverse direction. Let us then break the translational invariance by introducing a random on-site potential chosen from the range $[-25, 25]$ meV. In top panels of Fig. 4 we plot the probability current carried by K' (a), K (b) and by the edge mode (c) at the energy of 0.87 eV for a 30 nm long ribbon. Surprisingly we find that the probability density currents of the K' and K modes show breaking of the inversion symmetry along the $y = 0$ axis while the charge distribution preserves this symmetry to a good approximation. This can be understood considering that the modes are localized in different valleys that have opposite Berry curvatures which results in opposite \mathbf{v}_\perp . The broken translational symmetry now allows the electrons to scatter in the transverse direction. When the electrons are injected from the (pristine) left contact the modes polarized in K' are scattered preferably towards positive y values due to the positive v_y ($\Omega_z(K') < 0$). Therefore, we observe current circulating close to the top edge which results in nearly zero net current along the x -direction. The situation is opposite for the K polarized mode with the current depicted in (b) panel as $\Omega_z(K) = -\Omega_z(K')$. An

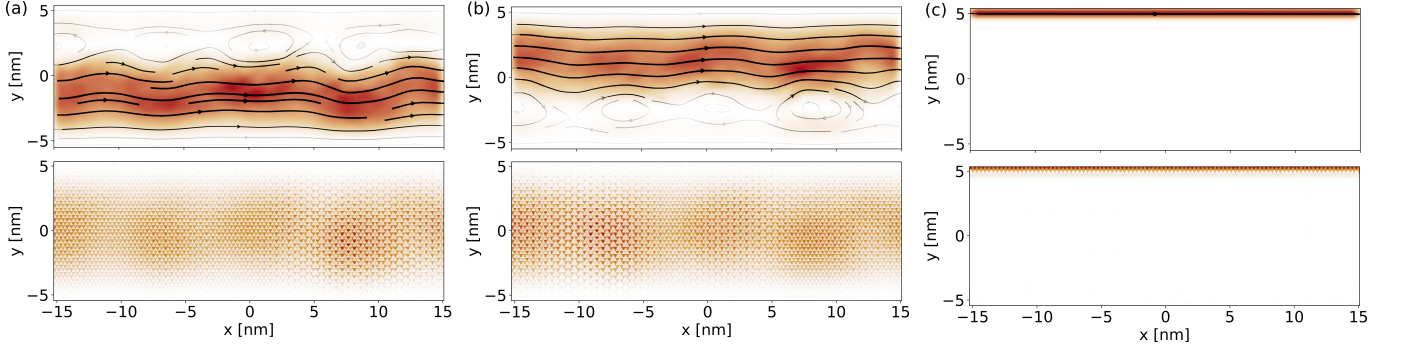


Figure 4. Top panels: the probability current obtained for K' (a), K (b) and edge (c) modes with the energy bands denoted in Fig. 1. Bottom panels: the corresponding probability densities.

analogous effect is obtained for a pristine ribbon, however there, the current asymmetry is accompanied by the current circulating around primitive cells of the lattice that preserves the translational symmetry.

For the edge mode presented in the panel (c) we see that both the current and the charge densities are localized at the edge of the ribbon accordingly to the analysis in Subsection II.1.1.

3. Stability of the valley polarization versus disorder

For a bulk MoS_2 the time-reversal symmetry protects from the inter-valley scattering by non-magnetic impurities. However, SOC is weak in the conduction band. As a result, when the Fermi energy lies above the minima of the two spin-opposite bands at K' and K points the scattering between bands of the same spin and the opposite valley is allowed. It was already shown for graphene nanoribbons that the inter-valley scattering is made possible by the presence of short-range scatterers^{43–45}. Let us now investigate how disorder in the form of atomic vacancies in the atomic lattice, acting as short-range scatterers, affect the valley polarization of the current and compare it to the bare electronic transport characterized by the mean free path.

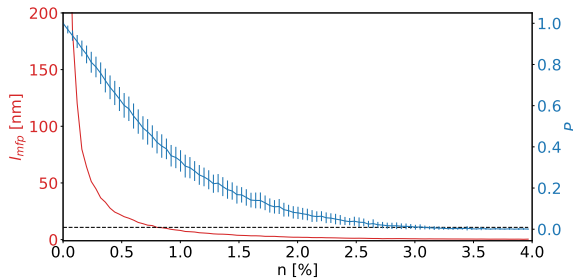


Figure 5. The mean free path (red curve) and the valley polarization (blue curve) versus abundance of vacancies.

Let us first inspect the mean free path which we calcu-

late according to the formula⁴⁶, $l_{\text{mfp}} = 2L \langle T_{\text{tot}} \rangle / \pi(N - \langle T_{\text{tot}} \rangle)$, where N is the number of current carrying modes at a given Fermi energy, L is the length of the considered scattering region (here 10 nm) and $\langle T_{\text{tot}} \rangle$ is the total transmission averaged over 100 realizations of the disorder at the Fermi energy of 0.9 eV.

The resulting mean free path versus the vacancy abundance is plotted in Fig. 5 with the red curve. We observe that when the abundance is increased from zero to 0.5% there is a rapid drop of l_{mfp} . This can be attributed to the Anderson localization^{47–49}. At around $n = 0.8\%$ l_{mfp} becomes smaller than the considered ribbon length (dashed line in Fig. 5) and the transport becomes diffusive. Finally, as the number of vacancies increases further, l_{mfp} saturates at the value of 0.4 nm.

Now, let us turn our attention to the valley polarization of the current which we estimate as:

$$P = \frac{\langle T_{K \rightarrow K} \rangle + \langle T_{K' \rightarrow K'} \rangle}{N_v}, \quad (8)$$

where N_v is the number of the valley polarized modes at the input of the ribbon and $\langle T_{K(\prime) \rightarrow K(\prime)} \rangle$ is an averaged transmission probability from K (K') to K (K') modes. For the considered Fermi energy we identify the valley polarization of the modes by inspecting the wave-vector corresponding to each mode. The resulting P is plotted in Fig. 5 with the blue curve along with its standard deviation. For a moderate vacancy concentration P drops, in a good approximation, linearly with n . As a result, even for a ribbon located deep in the ballistic regime, a moderate vacancy share is sufficient to distort the perfect valley polarization. At the transition region separating the ballistic and the diffusive transport, when $l_{\text{mfp}} \simeq L$, $P \simeq 0.4$ which is a signature of the strong valley mixing by the scatterers. As a result, we expect that the valley polarization of the current can be maintained only in the pristine samples where the vacancy concentration is less than 0.1 %. This is satisfied in MoS_2 samples obtained by mechanical exfoliation or by chemical vapour deposition for which the reported defects density is $3.5 \times 10^{13} \text{ cm}^{-2}$.⁵⁰

B. Gated nanoribbon

Very recently, it became possible to create locally gated MoS₂ nanostructures suitable for experimental quantum transport measurements^{14,15}. In this section we study a model system of a locally gated ribbon, i.e. a zigzag nanoribbon with a potential step along the x -direction.

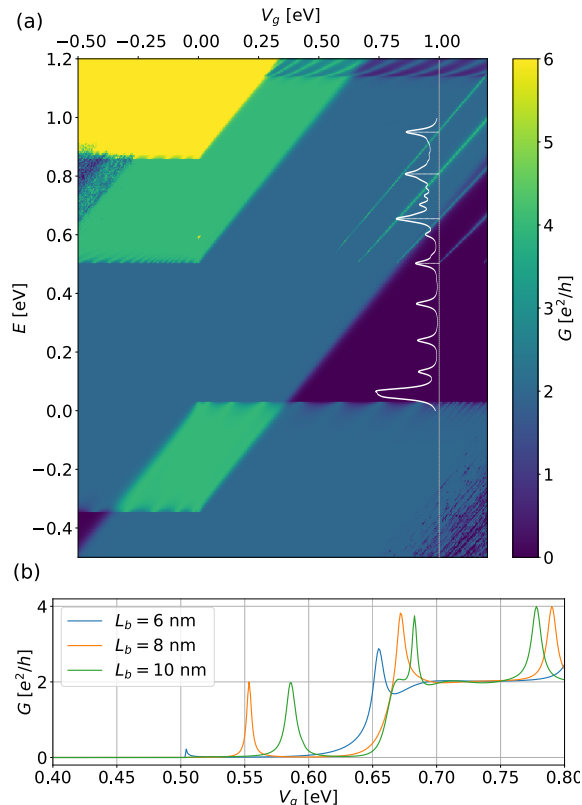


Figure 6. (a) Conductance map of a ribbon with a potential step as a function of the Fermi energy and the magnitude of the local potential. The white curve presents LDOS calculated in the potential barrier with peaks due to quasi-bound states originating from quasihole-edge states. (b) The conductance cross-section for $V_g = 1$ eV as a function of the the Fermi energy for three values of the barrier length.

The conductance as a function of the Fermi energy and V_g that controls the height of the potential step in the ribbon is presented in Fig. 6(a). Let us first focus on the case of a pristine ribbon with $V_g = 0$. In this case the conductance quantized in multiples of $2e^2/h$ is proportional to the number of current carrying modes at a given Fermi energy. For $E_f < 0.9$ eV the current is carried by the edge modes and we find stable plateaus of conductance. Such a stable conductance quantization was recently measured in WTe₂ nanodevices where it was a signature of the quantum spin Hall effect⁵¹—the two spin-opposite modes carried the topologically protected current on the opposite edges of the sample. Here, however, each edge band is Kramer-degenerate and consists of a doublet of counter propagating modes. This becomes

clear when we consider non-zero values of V_g that allow to gate-out the current. This happens e.g. for $E = 0.1$ eV and $V_g > 0.3$ eV. For such parameters, in the empty and the gated part of the nanostructure, the current is carried by different edges. As a result, for a finite width sample those edge current-carrying states are spatially disconnected and the transport through the ribbon is blocked despite its metallic character.

1. Resonant transport

In the map in Fig. 6(a) for $E > 0.5$ eV and $V_g > 0.5$ eV we observe a set of sharp lines of increased conductance. For this values of the Fermi energy, in the region of the ribbon far from the potential barrier, the current is carried by the edge mode located at the molybdenum edge [see Fig. 4(c)]. In the gated region the potential step shifts locally the chemical potential such that at the considered Fermi energy the current is also carried by the molybdenum edge but this time through a quasi-hole band. Such a potential landscape creates effectively a n-p-n junction where the gated region serves as an antidot in which quasi-bound quasi-hole states form. We confirm this by calculating local density of states for a system with disconnected leads and integrating it over the barrier region,

$$DOS_{\text{barrier}} = \sum_i \int_{-W/2}^{W/2} \int_{-L_b/3}^{L_b/3} |\Psi_i|^2 f_L(E, E_i, \Gamma) dx dy, \quad (9)$$

where f_L is a Lorentzian function with the width parameter $\Gamma = 0.02$ eV. The calculated density for $V_g = 1$ eV is plotted with the white curve overlaying the conductance map in Fig. 6(a). We observe maxima in the density of states that correspond to the edge states localized in the barrier region. They appear at the energies that correspond to the energies of the conductance resonances evidencing that the conductance increases when the incoming electron energy matches the energy of one of the quasi bound states. Similar resonances on a n-p-n junction were observed in bilayer graphene⁵² but here they are rather due to the localized edge states.

Another important feature of those states is their energy distribution. Note that the quasi-hole edge-band, out of which the quasi-bound states form, far from its maximum is approximately linear [see the spin-split bands that start around zero energy and are oriented towards valence bands in Fig. 1(b)]. The condition for the formation of the bound states is the quantization of the wave-vector $k = n\pi/W$ where n is an integer. As a result of the linear dependence of E on k for the quasi-hole band, the quasi-bound states are equidistant in energy. Accordingly, when we increase L_b we observe that the spacing between the resonances also rises as expected for bound states – see Fig. 6(b).

Note that the resonances are observed only for the Fermi energies for which the electrons are injected in a

band localized on the same edge as the quasi-bound edge states. As a result the resonances vanish below $E = 0.5$ eV. Despite this, we still find localized states in the anti-dot created by the barrier in this energy range.

2. Gate induced valley polarization of the current

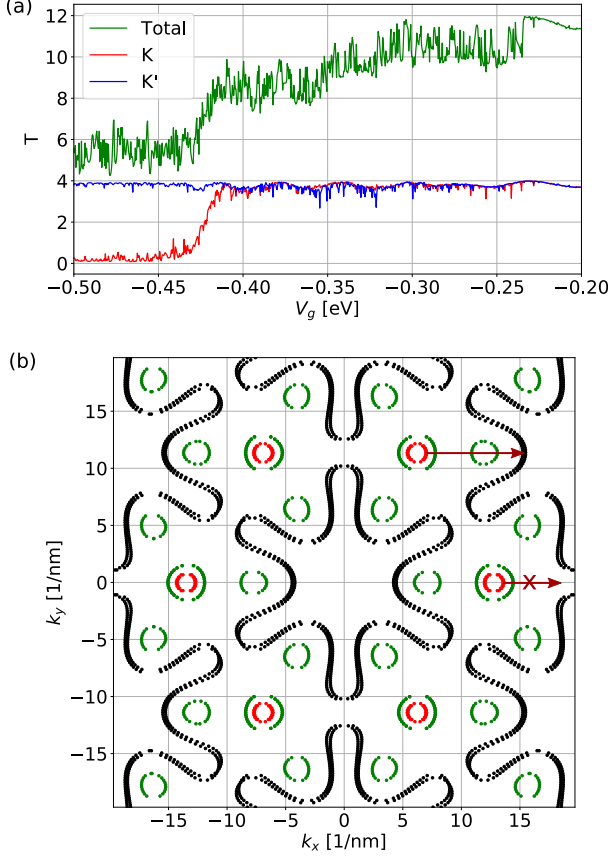


Figure 7. (a) The total transmission probability (green curve) for the Fermi energy $E = 0.9$ eV and the sums of transmission probabilities of K (red curve) and K' (blue curve) modes at the output of the locally gated ribbon. (b) Fermi contours at $E = 0.9$ eV (red), $E = 1$ eV (green) and $E = 1.35$ eV (black). The arrows present k_y scattering processes between the bands with a positive group velocity for an electron in the K' valley (straight arrow) and a forbidden process for an electron in the K valley (crossed arrow).

Let us now focus on the transport through the ribbon when the the Fermi energy lies above the conduction band minimum. Namely, we consider $E = 0.9$ eV and calculate the conductance for negative values of the local gate potential. The result is presented in Fig. 7(a) with the green curve which exhibits a sudden drop when the local gate potential reaches -0.42 eV.

We calculate the transmission probability to the K and K' modes at the right semi-infinite lead. The results are plotted with the red and the blue curves in Fig. 7(a)

Mode type	K'	K	edge
Transmission probability	0.991	0.025	0.103
	0.986	0.016	0.114
	0.976	0.089	0.337
	0.968	0.070	0.333

Table II. Transmission probabilities to the K' , K and edge modes for $V_g = -0.45$ eV.

respectively and the actual values of the transmission coefficient of the outgoing modes can be found in Table II for a single value of V_g . We observe that the conductance drop results from the almost completely blocked transport of K modes through the gated region. This results in a valley polarization of the current flowing from the structure with the polarization ratio being on average $P_v = |(T_K - T_{K'})|/T_{tot} = 75\%$.

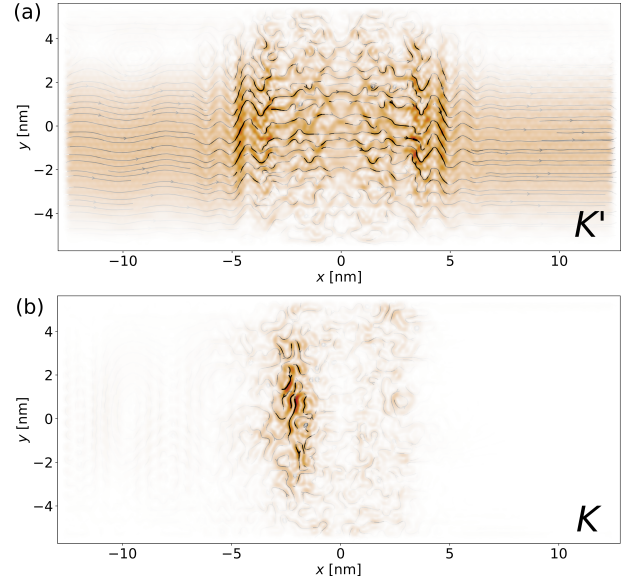


Figure 8. (a) The probability current for an electron injected in a K' valley polarized mode with a nonzero current distribution at the right lead. (b) The probability current for an electron injected in a K valley polarized mode that is reflected at the potential well.

The effect of the valley polarization can be understood by comparing the band structure in the gated region and in the region distant from the potential step. The potential step in the ribbon allows for reflection of the electrons propagating along the channel which results in the k_x momentum scattering. On the other hand, the ribbon is to a good approximation homogeneous along the y -direction making the scattering in k_y unlikely (recall that the bulk modes have well defined k_y values as can be seen in Fig. 2). If we now compare the Fermi contours for $E = 0.9$ eV that correspond to the empty region in the channel with the Fermi contours for $E = 1.35$ eV that correspond to the band structure in the gated region [see Fig. 7(b)] we observe that for the electrons injected in the K modes

there are no states with the positive group velocity at both energies that preserve k_y . On the other hand, such states do exist for the K' polarized modes. Therefore, the K' modes in the ribbon propagate freely through the gated region while the K modes are almost completely reflected which can be observed in Fig. 8. The small non-zero transmission probability of the K modes can be assigned to a small k_y momentum scattering which results from breaking of the mirror symmetry along the y -direction due to the presence of nonequivalent edges of the ribbon [see Fig. 8].

IV. SUMMARY

In this paper we studied the electronic transport in a MoS₂ nanoribbon. We characterized current carrying modes in a pristine ribbon demonstrating that despite finite width of the wire the modes are valley polarized and belong to K' , K and Q valleys depending on their wave vector. For the K and the K' polarized modes we found that the probability current is shifted towards the edges of the ribbon compatible with the valley Hall effect. In a disordered ribbon—populated by atomic vacancies—we found that the valley polarization drops linearly with the increase of the vacancy concentration and can drop below 0.5 even when the transport itself is still ballistic. We considered a model of a gated ribbon and found that

despite the metallic nature of the zigzag wire the current carried by the edge modes can be gated out and that in the gated region resonant quasi-hole edge states are formed. The latter results in sharp conductance peaks equidistant in energy due to the linear nature of the quasihole edge band. Finally, we found that by creating a negative potential step across the ribbon a nearly perfect valley polarization can be obtained due to the mismatch between the band structure near the K and the K' points.

ACKNOWLEDGMENTS

D.G., M.P. and M.P.N. acknowledge support within HOMING programme of the Foundation for Polish Science co-financed by the European Union under the European Regional Development Fund. D.C.S. was supported by CNCS-UEFISCDI, with project No. PN-III-P1-1.2-PCCDI-2017-0338. The calculations were performed on PL-Grid Infrastructure. The authors acknowledge helpful discussions with F. Piéchon, A. Akhmerov, M. Wimmer, J. Weston, D. Varjas and T. Rosdahl.

Appendix A: Hopping matrices

The inter-layer hopping matrices for the adopted TB model are as follows,

$$t_1^{MS} = \frac{\sqrt{2}}{7\sqrt{7}} \begin{pmatrix} -9V_{pd\pi} + \sqrt{3} V_{pd\sigma} & 3\sqrt{3} V_{pd\pi} - V_{pd\sigma} & 12V_{pd\pi} + \sqrt{3} V_{pd\sigma} \\ 5\sqrt{3} V_{pd\pi} + 3V_{pd\sigma} & 9V_{pd\pi} - \sqrt{3} V_{pd\sigma} & -2\sqrt{3} V_{pd\pi} + 3V_{pd\sigma} \\ -V_{pd\pi} - 3\sqrt{3} V_{pd\sigma} & 5\sqrt{3} V_{pd\pi} + 3V_{pd\sigma} & 6V_{pd\pi} - 3\sqrt{3} V_{pd\sigma} \end{pmatrix}, \quad (A1)$$

$$t_2^{MS} = \frac{\sqrt{2}}{7\sqrt{7}} \begin{pmatrix} 0 & -6\sqrt{3}V_{pd\pi} + 2V_{pd\sigma} & 12V_{pd\pi} + \sqrt{3}V_{pd\sigma} \\ 0 & -6V_{pd\pi} - 4\sqrt{3}V_{pd\sigma} & 4\sqrt{3}V_{pd\pi} - 6V_{pd\sigma} \\ 14V_{pd\pi} & 0 & 0 \end{pmatrix}, \quad (A2)$$

$$t_3^{MS} = \frac{\sqrt{2}}{7\sqrt{7}} \begin{pmatrix} 9V_{pd\pi} - \sqrt{3}V_{pd\sigma} & 3\sqrt{3}V_{pd\pi} - V_{pd\sigma} & 12V_{pd\pi} + \sqrt{3}V_{pd\sigma} \\ -5\sqrt{3}V_{pd\pi} - 3V_{pd\sigma} & 9V_{pd\pi} - \sqrt{3}V_{pd\sigma} & -2\sqrt{3}V_{pd\pi} + 3V_{pd\sigma} \\ -V_{pd\pi} - 3\sqrt{3}V_{pd\sigma} & -5\sqrt{3}V_{pd\pi} - 3V_{pd\sigma} & -6V_{pd\pi} + 3\sqrt{3}V_{pd\sigma} \end{pmatrix}. \quad (A3)$$

The intra-lattice hopping elements are,

$$t_1^{MM} = \frac{1}{4} \begin{pmatrix} 3V_{dd\delta} + V_{dd\sigma} & \frac{\sqrt{3}}{2} (-V_{dd\delta} + V_{dd\sigma}) & -\frac{3}{2} (V_{dd\delta} - V_{dd\sigma}) \\ \frac{\sqrt{3}}{2} (-V_{dd\delta} + V_{dd\sigma}) & \frac{1}{4} (V_{dd\delta} + 12V_{dd\pi} + 3V_{dd\sigma}) & \frac{\sqrt{3}}{4} (V_{dd\delta} - 4V_{dd\pi} + 3V_{dd\sigma}) \\ -\frac{3}{2} (V_{dd\delta} - V_{dd\sigma}) & \frac{\sqrt{3}}{4} (V_{dd\delta} - 4V_{dd\pi} + 3V_{dd\sigma}) & \frac{1}{4} (3V_{dd\delta} + 4V_{dd\pi} + 9V_{dd\sigma}) \end{pmatrix}, \quad (A4)$$

$$t_2^{MM} = \frac{1}{4} \begin{pmatrix} 3V_{dd\delta} + V_{dd\sigma} & \sqrt{3} (V_{dd\delta} - V_{dd\sigma}) & 0 \\ \sqrt{3} (V_{dd\delta} - V_{dd\sigma}) & V_{dd\delta} + 3V_{dd\sigma} & 0 \\ 0 & 0 & 4V_{dd\pi} \end{pmatrix}, \quad (A5)$$

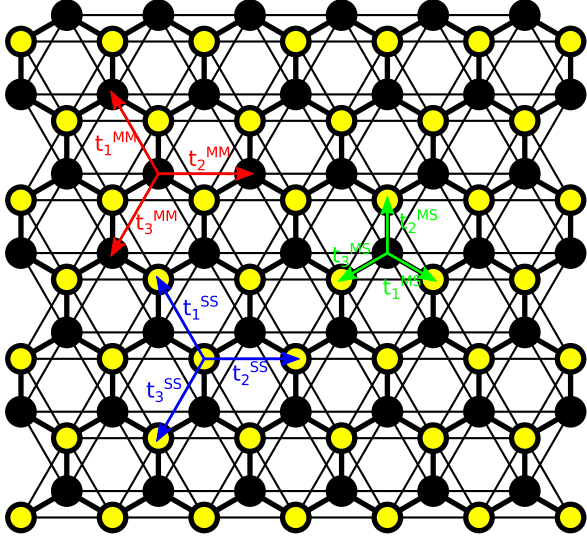


Figure 9. The lattice model for the considered system with denoted intra-lattice (red, blue arrows) and inter-lattice (green) hoppings.

$$t_3^{MM} = \frac{1}{4} \begin{pmatrix} 3V_{dd\delta} + V_{dd\sigma} & \frac{\sqrt{3}}{2}(-V_{dd\delta} + V_{dd\sigma}) & \frac{3}{2}(V_{dd\delta} - V_{dd\sigma}) \\ \frac{\sqrt{3}}{2}(-V_{dd\delta} + V_{dd\sigma}) & \frac{1}{4}(V_{dd\delta} + 12V_{dd\pi} + 3V_{dd\sigma}) & -\frac{\sqrt{3}}{4}(V_{dd\delta} - 4V_{dd\pi} + 3V_{dd\sigma}) \\ \frac{3}{2}(V_{dd\delta} - V_{dd\sigma}) & -\frac{\sqrt{3}}{4}(V_{dd\delta} - 4V_{dd\pi} + 3V_{dd\sigma}) & \frac{1}{4}(3V_{dd\delta} + 4V_{dd\pi} + 9V_{dd\sigma}) \end{pmatrix}, \quad (\text{A6})$$

$$t_1^{SS} = \frac{1}{4} \begin{pmatrix} 3V_{pp\pi} + V_{pp\sigma} & \sqrt{3}(V_{pp\pi} - V_{pp\sigma}) & 0 \\ \sqrt{3}(V_{pp\pi} - V_{pp\sigma}) & V_{pp\pi} + 3V_{pp\sigma} & 0 \\ 0 & 0 & 4V_{pp\pi} \end{pmatrix}, \quad (\text{A7})$$

$$t_2^{SS} = \frac{1}{4} \begin{pmatrix} V_{pp\sigma} & 0 & 0 \\ 0 & V_{pp\pi} & 0 \\ 0 & 0 & V_{pp\pi} \end{pmatrix}, \quad (\text{A8})$$

and

$$t_3^{SS} = \frac{1}{4} \begin{pmatrix} 3V_{pp\pi} + V_{pp\sigma} & -\sqrt{3}(V_{pp\pi} - V_{pp\sigma}) & 0 \\ -\sqrt{3}(V_{pp\pi} - V_{pp\sigma}) & V_{pp\pi} + 3V_{pp\sigma} & 0 \\ 0 & 0 & 4V_{pp\pi} \end{pmatrix}. \quad (\text{A9})$$

The mapping between the hoppings and the $t_{i,j}$ elements of the Hamiltonian Eq. 1 is presented in Fig. 9.

- ¹ S. Z. Butler, S. M. Hollen, L. Cao, Y. Cui, J. A. Gupta, H. R. Gutiérrez, T. F. Heinz, S. S. Hong, J. Huang, A. F. Ismach, E. Johnston-Halperin, M. Kuno, V. V. Plashnitsa, R. D. Robinson, R. S. Ruoff, S. Salahuddin, J. Shan, L. Shi, M. G. Spencer, M. Terrones, W. Windl, and J. E. Goldberger, *ACS Nano* **7**, 2898 (2013).
- ² A. K. Geim and I. V. Grigorieva, *Nature* **499**, 419 (2013).
- ³ Q. H. Wang, K. Kalantar-Zadeh, A. Kis, J. N. Coleman, and M. S. Strano, *Nat. Nanotechnol.* **7**, 699 (2012).
- ⁴ J. A. Wilson and A. D. Yoffe, *Advances in Physics* **18**, 193 (1969).
- ⁵ K. F. Mak, C. Lee, J. Hone, J. Shan, and T. F. Heinz, *Phys. Rev. Lett.* **105**, 136805 (2010).
- ⁶ A. Kuc, N. Zibouche, and T. Heine, *Phys. Rev. B* **83**, 245213 (2011).
- ⁷ O. Lopez-Sanchez, D. Lembke, M. Kayci, A. Radenovic, and A. Kis, *Nat. Nanotechnol.* **8**, 497 (2013).

- ⁸ S. Li, Y.-C. Lin, W. Zhao, J. Wu, Z. Wang, Z. Hu, Y. Shen, D.-M. Tang, J. Wang, Q. Zhang, H. Zhu, L. Chu, W. Zhao, C. Liu, Z. Sun, T. Taniguchi, M. Osada, W. Chen, Q.-H. Xu, A. T. S. Wee, K. Suenaga, F. Ding, and G. Eda, *Nature Mater* **17**, 535 (2018).
- ⁹ C. Yang, B. Wang, Y. Xie, Y. Zheng, and C. Jin, *Nanotechnology* **30**, 255602 (2019).
- ¹⁰ X. Liu, T. Xu, X. Wu, Z. Zhang, J. Yu, H. Qiu, J.-H. Hong, C.-H. Jin, J.-X. Li, X.-R. Wang, L.-T. Sun, and W. Guo, *Nat. Commun.* **4**, 1776 (2013).
- ¹¹ D. Kotekar-Patil, J. Deng, S. L. Wong, and K. E. J. Goh, *arXiv:1904.06983* (2019).
- ¹² D. Kotekar-Patil, J. Deng, S. L. Wong, C. S. Lau, and K. E. J. Goh, *Appl. Phys. Lett.* **114**, 013508 (2019).
- ¹³ B. Radisavljevic, A. Radenovic, J. Brivio, V. Giacometti, and A. Kis, *Nat. Nanotechnol.* **6**, 147 (2011).
- ¹⁴ B.-K. Kim, D.-H. Choi, T.-H. Kim, H. Kim, K. Watanabe,

- T. Taniguchi, H. Rho, Y.-H. Kim, J.-J. Kim, and M.-H. Bae, arXiv:1904.10295 [cond-mat] (2019).
- ¹⁵ X. Zheng, A. Calò, E. Albisetti, X. Liu, A. S. M. Alharbi, G. Arefe, X. Liu, M. Spieser, W. J. Yoo, T. Taniguchi, K. Watanabe, C. Aruta, A. Ciarrocchi, A. Kis, B. S. Lee, M. Lipson, J. Hone, D. Shahrjerdi, and E. Riedo, *Nat. Electron.* **2**, 17 (2019).
 - ¹⁶ C. H. Sharma and M. Thalakulam, *Sci. Rep.* **7**, 1 (2017).
 - ¹⁷ K. Marinov, A. Avsar, K. Watanabe, T. Taniguchi, and A. Kis, *Nat. Commun.* **8**, 1 (2017).
 - ¹⁸ C. Zhang, A. Johnson, C.-L. Hsu, L.-J. Li, and C.-K. Shih, *Nano Lett.* **14**, 2443 (2014).
 - ¹⁹ M. V. Bollinger, J. V. Lauritsen, K. W. Jacobsen, J. K. Nørskov, S. Helveg, and F. Besenbacher, *Phys. Rev. Lett.* **87**, 196803 (2001).
 - ²⁰ M. V. Bollinger, K. W. Jacobsen, and J. K. Nørskov, *Phys. Rev. B* **67**, 085410 (2003).
 - ²¹ Y. Li, Z. Zhou, S. Zhang, and Z. Chen, *J. Am. Chem. Soc.* **130**, 16739 (2008).
 - ²² A. A. Koós, P. Vancsó, G. Z. Magda, Z. Osváth, K. Kertész, G. Dobrik, C. Hwang, L. Tapasztó, and L. P. Biró, *Carbon* **105**, 408 (2016).
 - ²³ Z. Wang, H. Li, Z. Liu, Z. Shi, J. Lu, K. Suenaga, S.-K. Joung, T. Okazaki, Z. Gu, J. Zhou, Z. Gao, G. Li, S. Sanvito, E. Wang, and S. Iijima, *J. Am. Chem. Soc.* **132**, 13840 (2010).
 - ²⁴ X. Liu, T. Xu, X. Wu, Z. Zhang, J. Yu, H. Qiu, J.-H. Hong, C.-H. Jin, J.-X. Li, X.-R. Wang, L.-T. Sun, and W. Guo, *Nat. Commun.* **4**, 1776 (2013).
 - ²⁵ X. Xu, W. Yao, D. Xiao, and T. F. Heinz, *Nat. Phys.* **10**, 343 (2014).
 - ²⁶ W. Yao, D. Xiao, and Q. Niu, *Phys. Rev. B* **77**, 235406 (2008).
 - ²⁷ H. Yu, X. Cui, X. Xu, and W. Yao, *Natl. Sci. Rev.* **2**, 57 (2015).
 - ²⁸ G.-B. Liu, W.-Y. Shan, Y. Yao, W. Yao, and D. Xiao, *Phys. Rev. B* **88**, 085433 (2013).
 - ²⁹ A. Rycerz, J. Tworzydło, and C. W. J. Beenakker, *Nat. Phys.* **3**, 172 (2007).
 - ³⁰ T.-C. Hsieh, M.-Y. Chou, and Y.-S. Wu, *Phys. Rev. Materials* **2**, 034003 (2018).
 - ³¹ H. Rostami, R. Roldán, E. Cappelluti, R. Asgari, and F. Guinea, *Phys. Rev. B* **92**, 195402 (2015).
 - ³² E. Ridolfi, L. R. F. Lima, E. R. Mucciolo, and C. H. Lewenkopf, *Phys. Rev. B* **95**, 035430 (2017).
 - ³³ A. Heshmati-Moulai, H. Simchi, M. Esmailzadeh, and F. M. Peeters, *Phys. Rev. B* **94**, 235424 (2016).
 - ³⁴ F. Khoeini, K. Shakouri, and F. M. Peeters, *Phys. Rev. B* **94**, 125412 (2016).
 - ³⁵ J. Á. Silva-Guillén, P. San-Jose, and R. Roldán, *Applied Sciences* **6**, 284 (2016).
 - ³⁶ K. Kośmider, J. W. González, and J. Fernández-Rossier, *Phys. Rev. B* **88**, 245436 (2013).
 - ³⁷ C. W. Groth, M. Wimmer, A. R. Akhmerov, and X. Waintal, *New J. Phys.* **16**, 063065 (2014).
 - ³⁸ D. Gut and M. P. Nowak, 10.5281/zenodo.3465489.
 - ³⁹ A. Kormányos, V. Zólyomi, N. D. Drummond, P. Rakya, G. Burkard, and V. I. Fal'ko, *Phys. Rev. B* **88**, 045416 (2013).
 - ⁴⁰ T. Y. T. Hung, K. Y. Camsari, S. Zhang, P. Upadhyaya, and Z. Chen, *Science Advances* **5**, eaau6478 (2019).
 - ⁴¹ Z. Wu, B. T. Zhou, X. Cai, P. Cheung, G.-B. Liu, M. Huang, J. Lin, T. Han, L. An, Y. Wang, S. Xu, G. Long, C. Cheng, K. T. Law, F. Zhang, and N. Wang, *Nat. Commun.* **10**, 611 (2019).
 - ⁴² Y. Shimazaki, M. Yamamoto, I. V. Borzenets, K. Watanabe, T. Taniguchi, and S. Tarucha, *Nat. Phys.* **11**, 1032 (2015).
 - ⁴³ K. Wakabayashi, Y. Takane, and M. Sigrist, *Phys. Rev. Lett.* **99**, 036601 (2007).
 - ⁴⁴ K. Wakabayashi, Y. Takane, M. Yamamoto, and M. Sigrist, *New J. Phys.* **11**, 095016 (2009).
 - ⁴⁵ L. R. F. Lima, F. A. Pinheiro, R. B. Capaz, C. H. Lewenkopf, and E. R. Mucciolo, *Phys. Rev. B* **86**, 205111 (2012).
 - ⁴⁶ C. W. J. Beenakker, *Rev. Mod. Phys.* **69**, 731 (1997).
 - ⁴⁷ P. W. Anderson, *Phys. Rev.* **109**, 1492 (1958).
 - ⁴⁸ I. Klefogiannis, I. Amanatidis, and V. A. Gopar, *Phys. Rev. B* **88**, 205414 (2013).
 - ⁴⁹ E. Colomés and M. Franz, *Phys. Rev. Lett.* **120**, 086603 (2018).
 - ⁵⁰ J. Hong, Z. Hu, M. Probert, K. Li, D. Lv, X. Yang, L. Gu, N. Mao, Q. Feng, L. Xie, J. Zhang, D. Wu, Z. Zhang, C. Jin, W. Ji, X. Zhang, J. Yuan, and Z. Zhang, *Nat. Commun.* **6**, 1 (2015).
 - ⁵¹ S. Wu, V. Fatemi, Q. D. Gibson, K. Watanabe, T. Taniguchi, R. J. Cava, and P. Jarillo-Herrero, *Science* **359**, 76 (2018).
 - ⁵² M. Eich, R. Pisoni, H. Overweg, A. Kurzman, Y. Lee, P. Rickhaus, T. Ihn, K. Ensslin, F. Herman, M. Sigrist, K. Watanabe, and T. Taniguchi, *Phys. Rev. X* **8**, 031023 (2018).